Ore Geology Reviews 115 (2019) 103177

Contents lists available at ScienceDirect

Ore Geology Reviews

journal homepage: www.elsevier.com/locate/oregeorev

In-situ S and Pb isotope constraints on an evolving hydrothermal system, Tianbaoshan Pb-Zn-(Cu) deposit in South China

Shu-Cheng Tan[a], Jia-Xi Zhou[a,b,*], Mei-Fu Zhou[c], Lin Ye[b]

[a] School of Resource Environment and Earth Sciences, Yunnan University, Kunming 650500, China
[b] State Key Laboratory of Ore Deposit Geochemistry, Institute of Geochemistry, Chinese Academy of Sciences, Guiyang 550081, China
[c] Department of Earth Sciences, The University of Hong Kong, Hong Kong, China

ARTICLE INFO

Keywords:
In-situ S and Pb isotopes
An evolving hydrothermal system
Tianbaoshan Pb-Zn-(Cu) deposit
South China

ABSTRACT

The Upper Yangtze Pb-Zn metallogenic province in South China consists of > 400 carbonate-hosted Pb-Zn deposits within Neoproterozoic to Paleozoic strata. Origin of these deposits has been a matter of debate and is thought to be related to Proterozoic basement rocks, Paleozoic sedimentary rocks and the late Permian flood basalts of the Emeishan large igneous province (ELIP). The Tianbaoshan Pb-Zn-(Cu) deposit contains ~22Mt Pb-Zn ores @ 1.43 wt% Pb and 10.4 wt% Zn, and ~0.1Mt Cu ores @ 2.55 wt% Cu. Copper sulfide ores are composed dominantly of chalcopyrite and tetrahedrite, whereas Pb-Zn sulfide ores consist mainly of sphalerite and galena with minor chalcopyrite and tetrahedrite. In-situ $\delta^{34}S$ values (+3.2–+4.6‰) of chalcopyrite in the Cu ores are similar to the bulk $\delta^{34}S$ values (+3.9–+5.4‰) of chalcopyrite separates from the Cu ores and sphalerite separates (+1.7–+3.9‰) from the Pb-Zn ores. Such a sulfur isotope signature indicates that reduced sulfur of both the Cu and Pb-Zn ores was derived from a mixed source of magmatic sulfur (derived from igneous rocks) and sedimentary sulfur or evaporated marine sulfate by thermochemical sulfate reduction (TSR). In-situ Pb isotopic ratios of chalcopyrite grains in the Cu ores are similar to those of galena grains from both the Cu and Zn-Pb ores, suggesting that they have the same metal sources. Hence, our study demonstrates that both the Cu and Pb-Zn ores were co-genetic and their mineralizing elements were derived from or flowed through a mixed source of basement rocks and sedimentary rocks, and even basalts. The Tianbaoshan Pb-Zn-(Cu) deposit is an epigenetic sulfide deposit hosted in carbonate rocks and was formed from an evolving hydrothermal system from Cu to Pb-Zn.

1. Introduction

In the western Yangtze Block, South China (Fig. 1a), there are > 400 Pb-Zn deposits hosted in late Ediacaran to middle Permian carbonate rocks (e.g. Zhou et al., 2013a; Wang et al., 2014; Zhang et al., 2015), which form the giant Upper Yangtze Pb-Zn metallogenic province (Zhou et al., 2018a). Although the mineralization style of these Pb-Zn deposits is widely recognized as epigenetic, their origin are still debated (Zhou et al., 2018b). For example, the spatially association of these deposits with the late Permian flood basalts of the Emeishan large igneous province (ELIP) (Fig. 1b) led to classification of these as a distal magmatic hydrothermal deposits (e.g. Huang et al., 2010; Xu et al., 2014). In contrast, some studies interpreted these deposits as typical sedimentary exhalative (SEDEX) or sedimentary reworking (e.g. Zhu et al., 2018), because of the clearly strata-bound nature. However, other authors considered them to be MVT deposits because of similar ore-forming features (e.g. Zheng and Wang, 1991; Zhou et al., 2001). On the other hand, these Pb-Zn deposits are associated with Proterozoic basement rocks, Paleozoic sedimentary rocks and late Permian Emeishan flood basalts, some studies suggesting that they may represent a new type of carbonate-hosted epigenetic sulfide deposit (e.g. Zhou et al., 2014a, 2018b; Li et al., 2015; Tan et al., 2017; Wang et al., 2018). Hence, although these deposits are thought to be related to low temperature (< 250 °C) hydrothermal activities in the Triassic (Li et al., 2007; Zhou et al., 2013a, 2013b, 2015; Zhang et al., 2015; Hu et al., 2017), it has been long a matter of debate if they are the Mississippi-Valley type (MVT) deposits, because of the lack of precise ages of Pb-Zn mineralization (Zhou et al., 2013b).

Copper sulfide is not common in MVT deposits, although such an association is known from the world-class southeastern Missouri sulfide deposits in the USA (Burstein et al., 1993), the Wieloch sulfide deposits, Germany (Pfaff et al., 2009) and sulfide deposits in the Capricorn orogenic belt, Australia (Muhling et al., 2012). Here we report a rare example of the association of Cu and Pb-Zn in the Tianbaoshan deposit

* Corresponding author at: School of Resource Environment and Earth Sciences, Yunnan University, Kunming 650500, China.
E-mail address: zhoujiaxi@ynu.edu.cn (J.-X. Zhou).

https://doi.org/10.1016/j.oregeorev.2019.103177
Received 24 December 2018; Received in revised form 7 June 2019; Accepted 13 October 2019
Available online 15 October 2019
0169-1368/

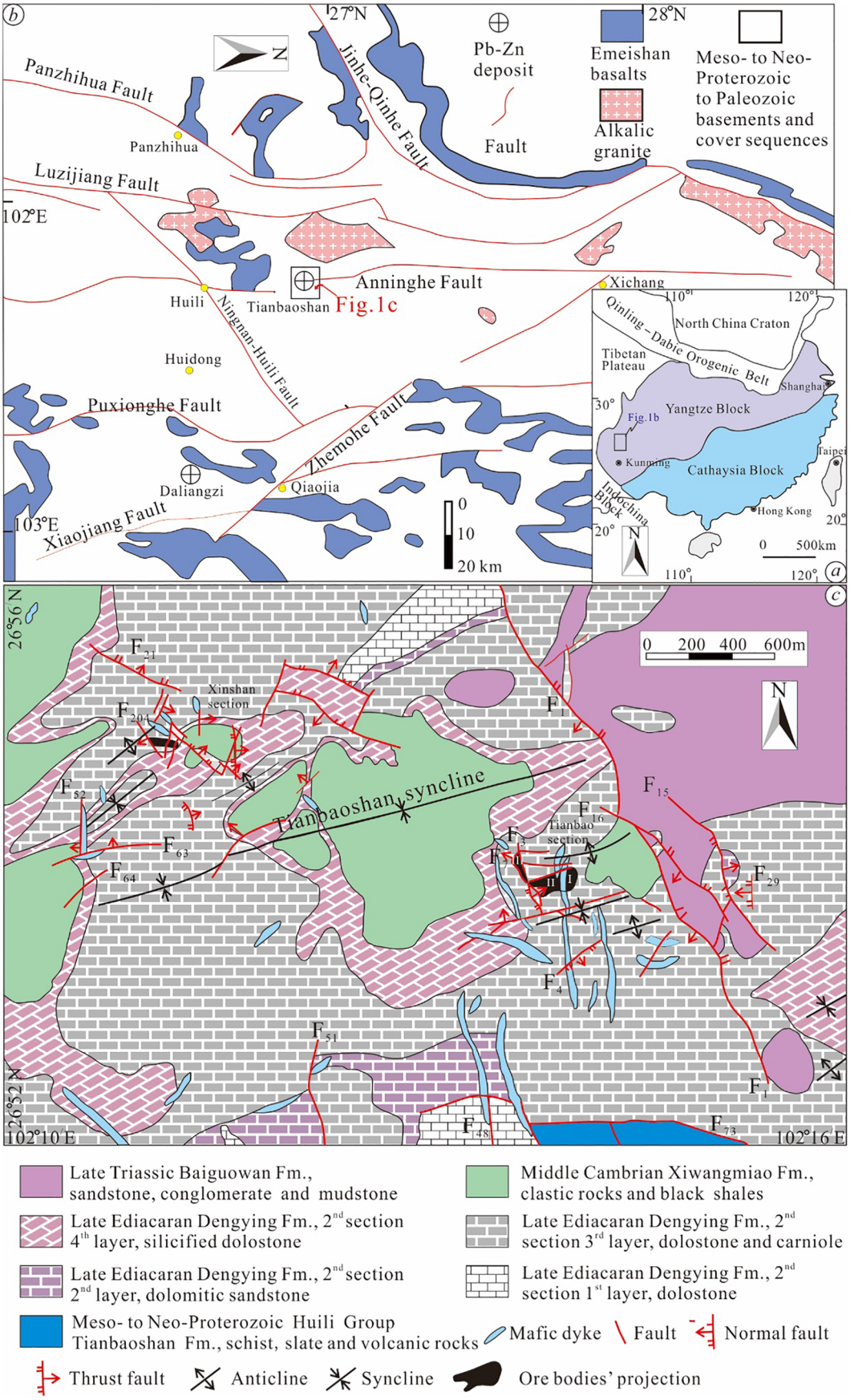

Fig. 1. (a) Regional geological setting of South China; (b) Sketch geological map of the Tianbaoshan region (after Wang et al., 2000); (c) Sketch geological map of the Tianbaoshan deposit (after Zhou et al., 2013c).

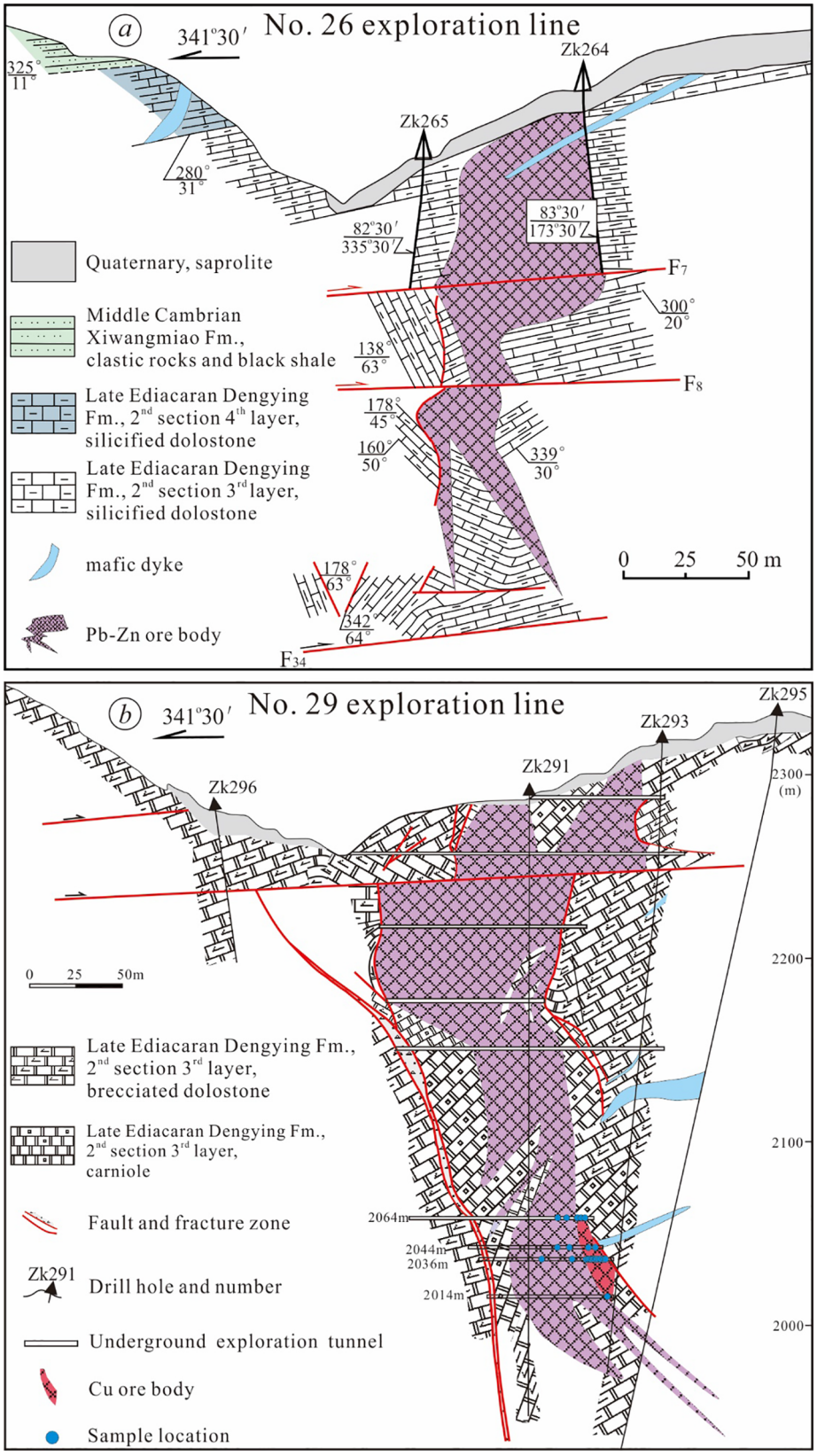

Fig. 2. Geological profiles of the Nos. 26 (a) and 29 (b) exploration lines in Tianbaoshan (modified from Wang et al., 2000; Zhou et al., 2013c).

of the upper Yangtze province, South China. In this deposit, co-existence of Cu and Pb-Zn ores (Fig. 2b) with enrichment of Cd, Ga and Ge has been previously noticed (Zhou et al., 2013c; Sun et al., 2016; Zhu et al., 2016). However, the significance of the Cu and Pb-Zn association in Tianbaoshan is not well illustrated in literature.

The recent development of micro-beam techniques has been widely used to study hydrothermal deposits (e.g. Ikehata et al., 2008; Chen et al., 2014; Zhang et al., 2014; Yuan et al., 2015; Bao et al., 2016). Particularly secondary iron mass spectrometry (SIMS) and laser ablation multi-collector inductively coupled plasma mass spectrometry (LA-

MC-ICPMS) are able to determine in-situ S and Pb isotopic compositions of sulfide minerals (e.g. Ushikubo et al., 2014; Jin et al., 2016; Bao et al., 2017; LaFlamme et al., 2016; Wang et al., 2018; Zhou et al., 2018c).

In this paper, we describe ore deposit geology and mineralogy of the Tianbaoshan deposit, and present bulk and NanoSIMS in-situ S isotopic data for chalcopyrite and sphalerite, and LA-MC-ICPMS in-situ Pb isotopic data for chalcopyrite and galena. These new datasets are used to constrain the origin of Cu and Pb-Zn ores, and their genetic relationship. We further propose a new metallogenic model for the Tianbaoshan Pb-Zn-(Cu) deposit. This study has significant implications for the formation of carbonate-hosted epigenetic sulfide deposits in the Upper Yangtze Pb-Zn metallogenic province and for the association of both Cu and Pb-Zn ores in general.

2. Geological background

2.1. Regional geology

The South China Block is composed of the Yangtze Block to the north and the Cathaysian Block to the south (Fig. 1a), both being amalgamated at around 820–850 Ma (Zhao et al., 2010; Wu et al., 2018). The Yangtze Block is bounded by the Tibetan Plateau to the west and by the Qinling-Dabie Orogenic belt to the north (Fig. 1a). The Yangtze Block consists of Archean crystalline basements, Meso- to Neo-Proterozoic folded basements (~1.7 Ga Dongchuan Group to ~1.1 Ga Huili/Kunyang Group and equivalents), overlain by the cover sequences of Paleozoic to early Mesozoic marine sediments and late Mesozoic to Cenozoic continental sediments (Sun et al., 2009; Qiu et al., 2016 and references therein). In the western Yangtze Block, the late Permian Emeishan flood basalts (~260 Ma) cover an area of > 0.5 $\times 10^6 km^2$ (Li et al., 2017). Cambrian to Triassic marine sediments contain abundant seawater sulfates and organic matter (Zhou et al., 2013b; Zhang et al., 2015). Two major events in South China are known as the Indosinian Orogeny (257–205 Ma) and Yanshanian Orogeny (205–65 Ma) (Faure et al., 2017 and references therein).

In the western Yangtze Block, > 400 Pb-Zn deposits comprise the Upper Yangtze Pb-Zn metallogenic province that covers an area of > $0.2 \times 10^6 km^2$ and are hosted within late Ediacaran to middle Permian carbonate rocks (e.g. Cromie et al., 1996; Wang et al., 2014; Zhang et al., 2015; Hu et al., 2017; Zhou et al., 2018b). They were likely formed in the late Triassic (230–200 Ma) on the basis of sulfide Rb-Sr, calcite/fluorite Sm-Nd and bitumen Re-Os isotopic dating (Zhou et al., 2018a and references therein). The association of independent Cu ores and Pb-Zn ores is rare in the Upper Yangtze province, but micro-grain chalcopyrite in Pb-Zn ores is common, for example in the Huize and Fule deposits (Li et al., 2007; Zhou et al., 2018b).

2.2. Local Geology

The Tianbaoshan Pb-Zn-(Cu) deposit is located about 50 km north of Huili, southwestern Sichuan Province (Fig. 1b). In this region, the Meso- to Neo-Proterozoic Huili Group Tianbaoshan Formation consists mainly of schist, slate, metamorphosed acidic volcanic lava and tuff (Wang et al., 2000). The late Ediacaran Dengying Formation is composed dominantly of dolostone and is > 1000 m in thickness (Zhou et al., 2013c). The Dengying Formation in Tianbaoshan (Fig. 1c and 2a-b) has four layers (Zhang, 2017). The 1st layer, up to 320 m thick, consists of dolostone; the 2nd layer is 32–112 m in thickness and is made up of dolomitic sandstone; the 3rd layer, 240–470 m thick, is composed of silicified, brecciated and cavernous dolostone (Fig. 2a-b), which host oxidized and primary sulfide ores (Fig. 3a-f); and the 4th layer is < 160 m thick and consists of gray-white silicified dolostone. The overlying middle Cambrian Xiwangmiao Formation is dominated by clastic rocks rich in black shales and evaporated sulfates (Zhou et al., 2013c). The late Triassic Baiguowan Formation is composed mainly of sandstone, mudstone and conglomerate (Fig. 1c).

In Tianbaoshan, NS- and EW-trending faults are dominant, and the NE- and NW-trending faults are secondary (Fig. 1c). The NS-trending Anninghe structural zone is a regional tectonic belt (Fig. 1b) that controls the distribution of some carbonate-hosted Pb-Zn deposits, of which the Tianbaoshan deposit is structurally controlled by its secondary fault (F_1 in Fig. 1c). The NNW-trending F_1 fault dips 60°–85°. This fault records changes in stress from extension to compression, then to left-lateral transgression, and finally to compression (Wang et al., 2000; Zhang et al., 2006). The NW-trending faults (F_3, F_7 and F_{204} in Fig. 1c and 2a-b) crosscut ore bodies dip > 80° to NE (Fig. 1c). The Tianbaoshan syncline has a sharp north limb and broad-gradual asymmetric multiple syncline (Fig. 1c). Its axis trends NEE with dipping angles of 30°–50° and 20° for the north and south limbs, respectively. Previous studies divided the tectonic stress fields in Tianbaoshan into the late Indosinian and early Yanshanian two groups, corresponding to the maximum compressive stress direction of 290°–110° and 20°–30° or 200°–210°, respectively (Zhang et al., 2006). The stress state changed from being compressive in the late Indosinian to extensional in the early Yanshanian (Wang et al., 2000; Zhang et al., 2006; Qiu et al., 2016; Faure et al., 2017). This shift in stress generated the necessary structures that control the formation and locations of Cu and Pb-Zn ore bodies in Tianbaoshan.

Proterozoic alkali granites, acidic volcanic lava and tuff (*ca.* 1 Ga; Geng et al., 2007), Permian basalts (*ca.* 260 Ma; Zhou et al., 2002) and Mesozoic mafic dykes, which are part of the ELIP, are widely distributed in this region (Fig. 1b). However, in Tianbaoshan, only Mesozoic mafic dykes are observed (Figs. 1c and 2a-b), including lamprophyre (odinite and spessartite), diabase, gabbro-diabase and olivine-diabase (Wang et al., 2000), of which diabase dykes are dominant (Figs. 1c and 2a-b) and contain zircons with U-Pb ages of 156–166 Ma (Zhang, 2017). These mafic dykes occur along the NS- and NW-trending faults with a width of 20–30 m, and are close to or cross-cut sulfide ore bodies (Fig. 1c and 2a-b).

3. Ore deposit geology

Sulfide ore bodies occur in dolostone of the Dengying Formation and are crosscut by NW-trending concealed fractures (Fig. 1c). Underground mining and exploratory drilling provide excellent access to two ore sections (Tianbao and Xinshan) with one Cu and two main Pb-Zn ore bodies (Fig. 2a-b). The Cu and Pb-Zn ores are stratiform and occur as tabular, lenticular and pipe-like bodies with sharp boundaries against the ore-hosting rocks (Figs. 2a-b and 3a-f).

3.1. Pb-Zn sulfide ore bodies

The largest sulfide Pb-Zn ore body in Tianbao section was cut into three segments (i.e. Nos. I, II and III) by F_3 fault and mafic dykes (Fig. 1c). These segments have similar morphology and occur as veins or cylinder-shaped bodies with many branches (Fig. 2a-b). Nos. I + II segments of the Tianbao ore body are 400 m in depth, 285 m in length and 2.1–50 m in width (Zhou et al., 2013c). These two segments contain 18Mt Pb + Zn ore reserves with grades of 1.28–2.5 wt% Pb and 7.76–10.1 wt% Zn, and the mean ratio of Zn/(Zn + Pb) is 0.87 (Wang et al., 2000). In addition, the Pb-Zn ores contain 90.2–96.3 g/t Ag and are rich in several other elements, resources totaling 7.3kt Cd, 258 t Ga, 122 t Ge, and 20 t In (Zhu et al., 2016). These elements are mainly hosted in sphalerite, replacing Zn by isomorphism (Zhou et al., 2011; Zhu et al., 2016).

3.2. Cu sulfide ore body

Recently, a Cu ore body has been discovered between 2064 and 2014 m (Fig. 2b) levels below the Nos. I + II segments of the Pb-Zn ore body (Fig. 3j-l). The boundary of these two types of ore body hasn't been observed. The strike extent of the Cu ore body is similar to that of Nos. I + II segments of the Pb-Zn ore body (Fig. 2b). The Cu ore body is

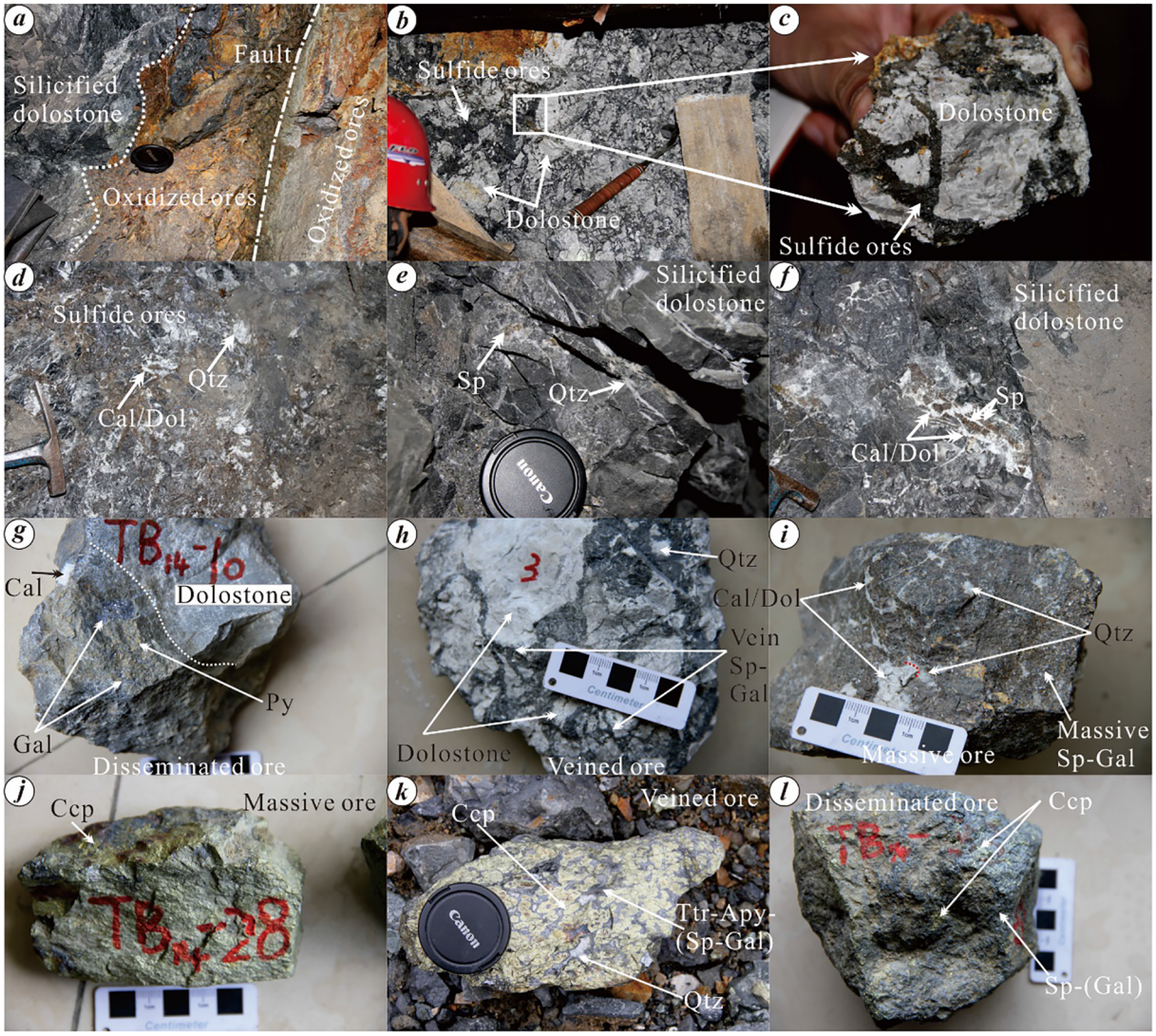

Fig. 3. (*a*) Field photograph shows the boundary between oxidized ores and silicified dolostone, and a fault; (*b-c*) Veined sulfide ores and brecciated dolostone; (*d*) Veined calcite (Cal) and fine-grained Cal and quartz (Qtz) within sulfide ores; (*e*) Disseminated sphalerite (Sp) and veined Qtz within silicified dolostone; (*f*) Veined Cal and Sp within silicified dolostone; (*g*) The boundary between sulfide ores and dolostone; (*h*) Veined Sp and galena (Gal) within brecciated dolostone; (*i*) Veined Cal within Sp and Gal aggregates; (*j*) Coarse-grained chalcopyrite (Ccp) aggregates; (*k*) Veined tetrahedrite (Ttr), arsenopyrite (Apy), Sp and Gal aggregates fill into brecciated Ccp; (*l*) Disseminated Ccp within Sp and Gal aggregates. Abbreviations refer to Whitney and Evans (2010).

50 m in depth extent and 2–15 m in width, and contains > 0.1Mt Cu ore reserves with a mean grade of 2.55 wt% Cu (Sun et al., 2016).

3.3. Mineralogy and mineral paragenesis

3.3.1. Pb-Zn sulfide ores

Sulfide Pb-Zn ores consist mainly of sphalerite and galena, secondary pyrite, chalcopyrite and tetrahedrite, with calcite, dolomite and quartz as gangue minerals (Figs. 3d-I and 4a-f). Pb-Zn sulfide ores have massive, disseminated, veined or banded structures (Fig. 3b-i). Sphalerite and galena display granular and cataclastic textures (Fig. 5a-l). It is worth noting that in the Pb-Zn ores, chalcopyrite disease structure (Barton and Bethke, 1987) in sphalerite is common (Fig. 4f), which may be related to exsolution of chalcopyrite from sphalerite during cooling or replacement of original Fe-bearing sphalerite by an aggregate of chalcopyrite (Barton and Bethke, 1987).

3.3.2. Cu sulfide ores

Sulfide Cu ores consist mainly of chalcopyrite, tetrahedrite and arsenopyrite, minor galena, sphalerite and pyrite, with quartz as gangue mineral (Fig. 3j-l, 4g-l and 5a-l). These Cu ores have massive, veined or disseminated structures (Fig. 3j-l). Sphalerite in the Cu ores occurs as granular forms coexisting with chalcopyrite or is enclosed by chalcopyrite grains, while galena fills fractures in chalcopyrite grains. Tetrahedrite and arsenopyrite in the Cu ores occur as micro-veinlets or grains enclosed by other sulfides (Figs. 4g-l and 5a-l).

3.4. Paragenetic sequence of mineralization and alteration

The hydrothermal activity can be divided into sulfide + (quartz + carbonates) and quartz + carbonates two ore-forming stages. The sulfide stages include (i) Cu ores, chalcopyrite-dominant, with lesser tetrahedrite, arsenopyrite, sphalerite, galena and pyrite, and (ii) Pb-Zn ores, sphalerite-dominant, with lesser galena, pyrite and chalcopyrite (Fig. 3g-l). There are three generations of chalcopyrite, sphalerite and galena in the two types of ores (Figs. 4 and 5). Chalcopyrite-I is fine grained and is enclosed by tetrahedrite (Figs. 4h-i, l and 5h-i) and/or sphalerite-II (Fig. 4l). It also coexists with tetrahedrite, arsenopyrite, sphalerite-I and galena-I (Fig. 5h). Chalcopyrite-II is coarse grained and coexists with tetrahedrite (Fig. 4g) and sphalerite-II (Fig. 4j, l), or includes tetrahedrite and arsenopyrite

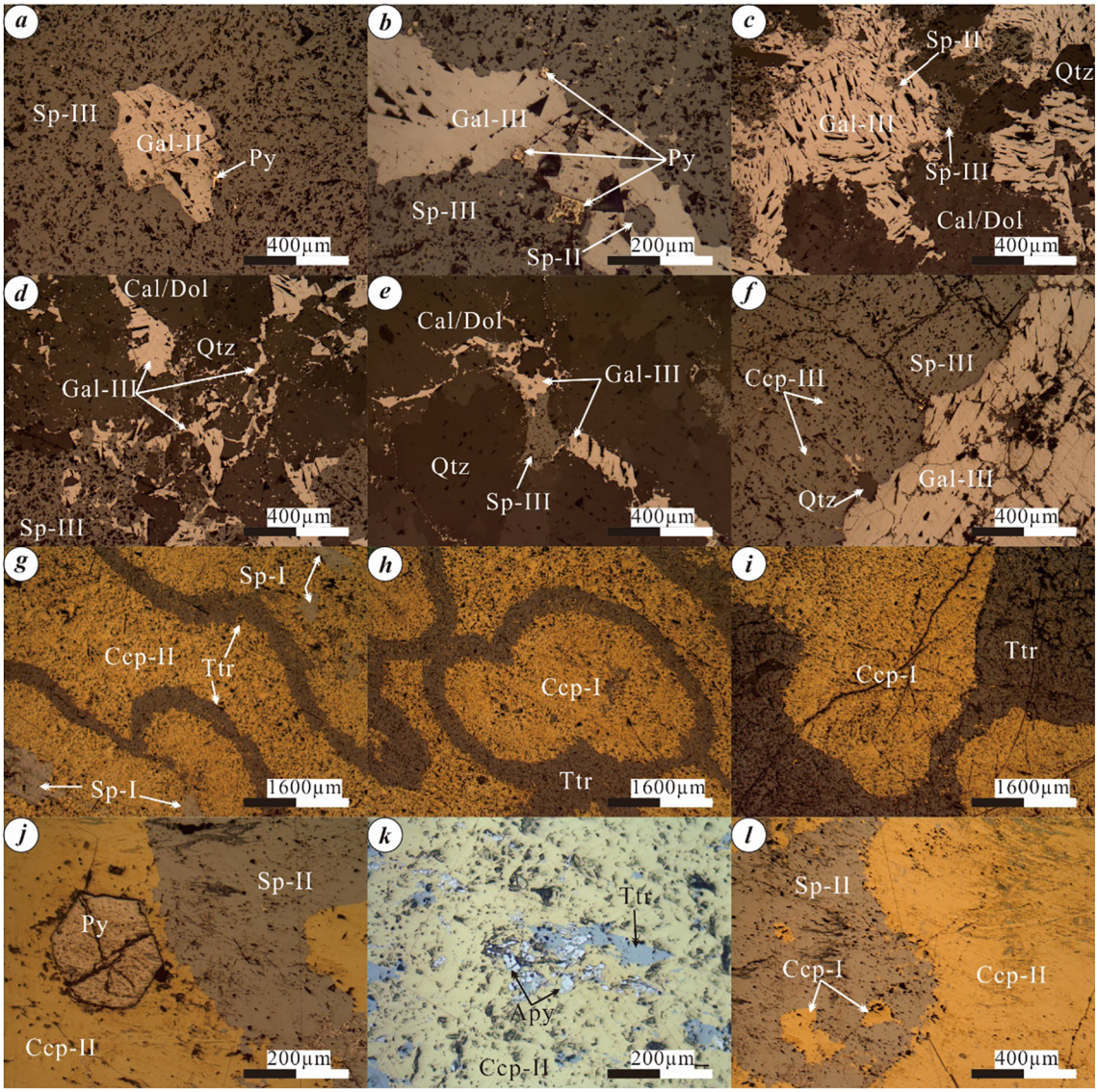

Fig. 4. (*a*) Granular galena (Gal-II) coexists with fine-grained pyrite (Py) and is enclosed by sphalerite (Sp-III); (*b*) Sp-II is included in Gal-III that coexists with fine-grained Py and Sp-III; (*c*) Sp-II is contained by Gal-III that coexists with Sp-III, calcite (Cal) and quartz (Qtz); (*d*) Veined Gal-III fills into Cal and Qtz, and coexist with Sp-III; (*e*) Veined Gal-III and granular Sp-III fill into Cal and Qtz; (*f*) Disseminated chalcopyrite (Ccp-III) within Sp-III that coexists with Gal-III and Qtz; (*g*) Fine-grained Sp-I is enclosed in Ccp-II that is packed by veined tetrahedrite (Ttr); (*h*) Granular Ccp-I is wrapped by Ttr; (*i*) Granular Ccp-I coexists with Ttr; (*j*) Granular Py is included in Ccp-II that coexists with Sp-II; (*k*) Fine-grained Ttr and arsenopyrite (Apy) are wrapped by Ccp-II; (*l*) Granular Ccp-I is enclosed in Sp-II that coexists with Ccp-II. Abbreviations refer to Whitney and Evans (2010).

(Fig. 4k and 5a-g, j-l), and sphalerite-I (Fig. 4g). Chalcopyrite-III presents as fine grains within sphalerite-III (Fig. 4f). Sphalerite-I is fine grained and is enclosed by chalcopyrite-II (Fig. 4j) and/or coexists with chalcopyrite-I (Fig. 5h). Sphalerite-II shows granular texture and coexists with chalcopyrite-II (Fig. 4j, l and 5k) and/or is surrounded by galena-III (Fig. 4b-c). Sphalerite-III is coarse grained and includes granular galena-II and pyrite (Fig. 4a), and/or coexists with galena-III (Fig. 4b-f) and chalcopyrite-III (Fig. 4f). Galena-I occurs as a fine grained aggregates and is enclosed by tetrahedrite and chalcopyrite-II (Fig. 5b-c, e-h). Galena-II has a granular and corrugated texture and is enclosed by sphalerite-III (Fig. 4a) and/or coexists with chalcopyrite-II (Fig. 5l). Galena-III occurs as corrugated texture and coexists with sphalerite-III (Fig. 4b-f), and/or veined aggregate inserts in tetrahedrite, chalcopyrite-I and chalcopyrite-II (Fig. 5a-d, k). More details about mineral paragenesis are listed in Table 1.

Wall rock alteration includes carbonate (calcite and dolomite), silicate, chlorite and ferrite. These alteration styles can be divided into two stages: (i) the pre-ore alteration stage of carbonate, silicate and chlorite that formed veined calcite/dolomite, banded silicification or silicified dolostone (Fig. 3a, e, f) and chlorite (Zhang, 2017), respectively, and (ii) the post-ore alteration stage of carbonate, silicate and ferrite that formed fine veined calcite/dolomite, quartz and oxidized ores (Fig. 3a), respectively. These altered minerals are a zoned from ores to wall rocks, i.e. from sulfide or oxidized ores to chlorite, then to quartz or silicified dolostone, and then to quartz veinlets (Zhou et al., 2013c; Zhang, 2017).

4. Samples and analytical methods

Fifty samples were collected mainly from the Cu ores (Fig. 2b) and Pb-Zn ores. Eleven chalcopyrite and 1 sphalerite separates were chosen from these Cu ores, and 4 sphalerite separates were collected from the Pb-Zn ores by micro-drill for bulk sulfur isotope analysis. Six thin sections of the Cu and Pb-Zn ores were used for in-situ S and Pb isotope analyses. Analyses of bulk and in-situ S isotopes were completed at the Institute of Geochemistry, and Institute of Geology and Geophysics, Chinese Academy of Sciences, respectively. Analysis of in-situ Pb

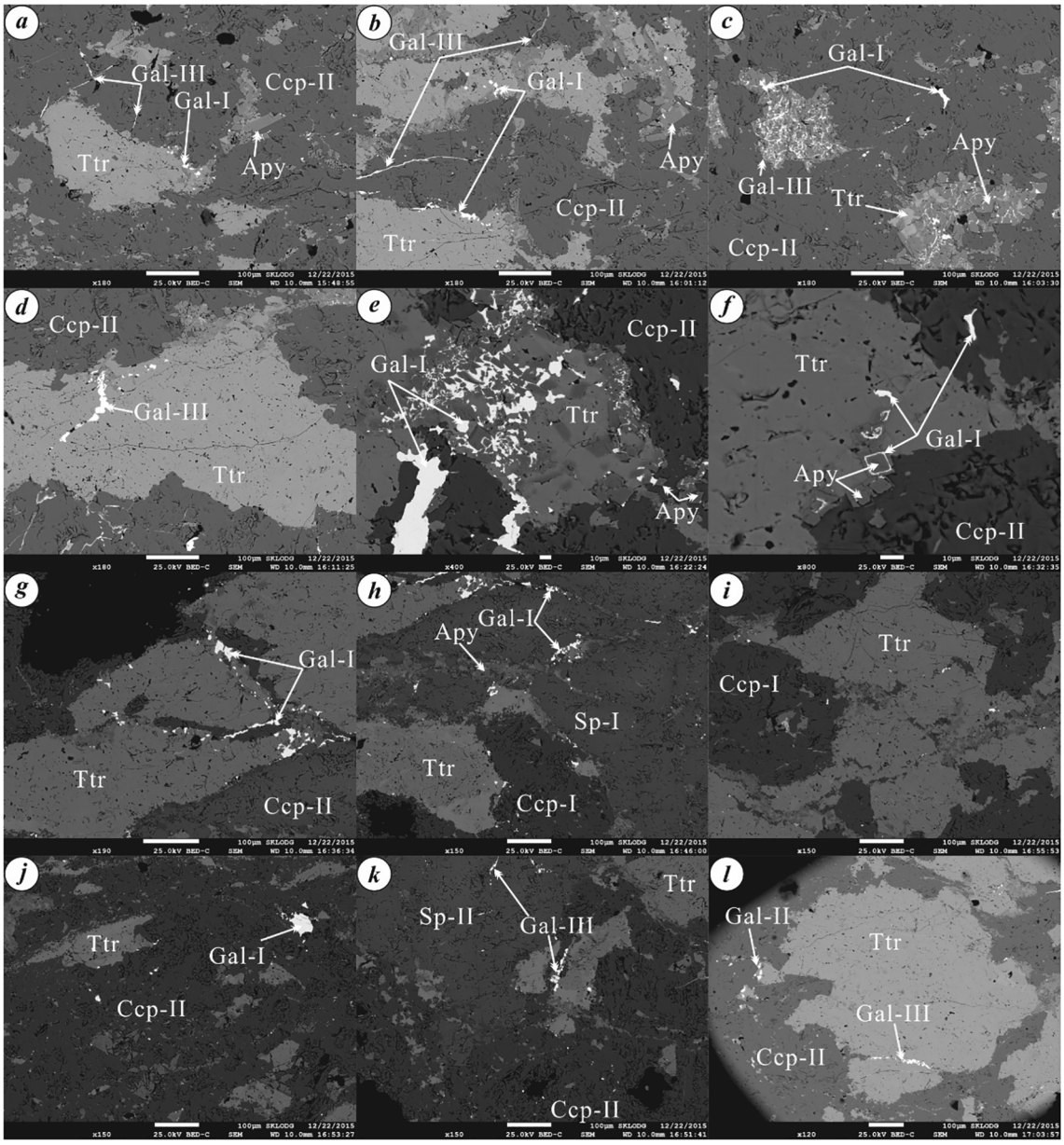

Fig. 5. (*a-c*) Granular galena (Gal-I) coexists with tetrahedrite (Ttr), together with granular arsenopyrite (Apy) are enclosed in chalcopyrite (Ccp-II), which is packed by veined Gal-III; (*d*) Veined Gal-III fills into Ttr that coexists with Ccp-II; (*e*) Gal-I aggregates and granular Apy within Ttr that coexists with Ccp-II; (*f*) Granular Apy is wrapped by Gal-I that is enclosed by Ttr and Ccp-II; (*g*) Fine-grained Gal-I is included by Ttr that coexists with Ccp-II; (*h*) Granular Ccp-I, Sp-I, Gal-I and Ttr coexist with granular Apy; (*i*) Franular Ccp-I coexists with Ttr; (*j*) Granular Gal-I and Ttr is enclosed by granular Ccp-II; (*k*) Veined Gal-III is included by Sp-II that coexists with Ccp-II; (*l*) Granular Gal-II coexists with Ccp-II and veined Gal-III fills into Ttr. Abbreviations refer to Whitney and Evans (2010).

isotopes was carried out at the State Key Laboratory of Continental Dynamics, Northwest University. The detailed analytical methods are listed in Appendix A.

5. Analytical results

5.1. Sulfur isotopic compositions

Bulk and in-situ sulfur isotopic compositions of chalcopyrite and sphalerite are presented in Table 2, and Figs. 6e-f and 7a-b. Chalcopyrite crystals have NanoSIMS in-situ $\delta^{34}S$ values of +3.2–+4.6‰ (Fig. 6e-f); Chalcopyrite and sphalerite separates have bulk $\delta^{34}S$ values of +1.7–+5.5‰ (Table 2), of which the former has $\delta^{34}S$ values of +3.9–+5.5‰ and the latter has $\delta^{34}S$ values ranging from +1.7 to +3.9‰ (Fig. 7a). Among these data, chalcopyrite-I and chalcopyrite-II separates have $\delta^{34}S$ values ranging from +3.2 to +4.6‰ and +5.2 to +5.5‰, respectively; sphalerite-II and sphalerite-III separates have $\delta^{34}S$ values of +1.7‰ and +2.9–+3.9‰, respectively (Fig. 7b).

5.2. In-situ Pb isotopic ratios

In-situ Pb isotopic ratios of chalcopyrite and galena are presented in Table 3 and Figs. 8 and 9. Sulfide crystals have in-situ $^{206}Pb/^{204}Pb$ = 18.43–18.48, $^{207}Pb/^{204}Pb$ = 15.72–15.77 and $^{208}Pb/^{204}Pb$ = 38.77–38.93 with μ ($^{238}U/^{204}Pb$) values of 9.7–9.8 (Zartman and Doe, 1981), of which chalcopyrite crystals have in-situ $^{206}Pb/^{204}Pb$ ratios of 18.43–18.48, $^{207}Pb/^{204}Pb$ ratios of 15.72–15.76 and $^{208}Pb/^{204}Pb$ ratios of 38.78–38.89, and galena crystals have in-situ $^{206}Pb/^{204}Pb$ = 18.44–18.48, $^{207}Pb/^{204}Pb$ = 15.74–15.77 and $^{208}Pb/^{204}Pb$ = 38.77–38.93. In-situ Pb isotopic ratios of chalcopyrite-I,

Table 1
Mineral paragenesis in the Tianbaoshan Pb-Zn-(Cu) deposit, South China.

Period	Hydrothermal				Supergene
Stage	Sulfide-(Qtz-carbonates)			Qtz-carbonates	Oxidized Leached
Mineral assemblage	Ccp + Ttr + Apy + (Sp + Gal) + Qtz + Dol/Cal		Sp + Gal + Qtz + Dol/Cal	Qtz + Dol + Cal	
Mineral paragenesis	I	II	III	IV	V

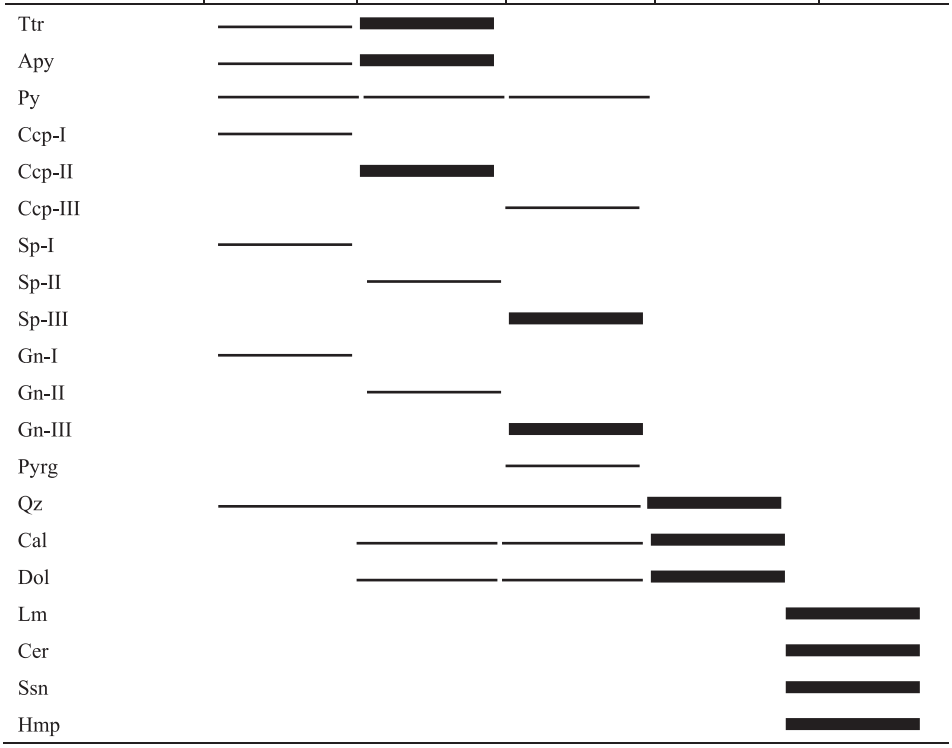

Ttr-tetrahedrite; Apy-arsenopyrite; Py-pyrite; Ccp-chalcopyrite; Gal-galena; Sp-sphalerite; Pyrg-pyrargyrite; Qtz-quartz; Cal-calcite; Dol-dolomite; Lm-limonite; Cer-cerussite; Ssn-smithsonite; Hmp-hemimorphite. Abbreviations refer to Whitney and Evans (2010). —— Less; ▬ More.

Table 2
Sulfur isotopic compositions of the Tianbaoshan Pb-Zn-(Cu) deposit, South China.

No.	Location/Mineral	$\delta^{34}S_{CDT}$/‰	Note
TB_{14}-4-01	2064m, Ccp-I	+4.6	NanoSIMS in situ
TB_{14}-4-02	2064m, Ccp-I	+3.9	
TB_{14}-4-03	2064m, Ccp-I	+4.0	
TB_{14}-40-01	2014m, Ccp-I	+3.2	
TB_{14}-4	2064m, Ccp-I	+4.16	Bulk
TB_{14}-21	2036m, Ccp-II	+5.18	
TB_{14}-23	2036m, Ccp-II	+5.38	
TB_{14}-24	2036m, Ccp-II	+5.34	
TB_{14}-27	2036m, Ccp-II	+5.43	
TB_{14}-28	2036m, Ccp-II	+5.41	
TB_{14}-28*	2036m, Ccp-II	+5.40	
TB_{14}-32	2036m, Ccp-II	+5.25	
TB_{14}-34	2064m, Ccp-II	+5.54	
TB_{14}-35	2036m, Ccp-II	+5.38	
TB_{14}-36	2036m, Ccp-I	+4.12	
TB_{14}-40	2014m, Ccp-I	+3.93	
TB_{14}-2	2064m, Sp-III	+3.88	
TB_{14}-2*	2064m, Sp-III	+3.82	
TB_{14}-7	2044m, Sp-II	+1.69	
TB_{14}-9	2044m, Sp-III	+3.44	
TB_{14}-12	2036m, Sp-III	+2.86	
TB_{14}-20	2036m, Sp-III	+3.31	

Ccp-chalcopyrite; Sp-sphalerite.
*Samples are used for procedural repeats.

chalcopyrite-II, galena-I, galena-II and galena-III are listed in Table 3 and are shown in Figs. 8 and 9.

6. Discussion

6.1. An involving hydrothermal system

The newly-discovered Cu ores in Tianbaoshan contain granular sphalerite grains that coexist with or are enclosed by aggregate chalcopyrite (Figs. 4 and 5), suggesting that in the Cu ores, sphalerite-I formed simultaneously with chalcopyrite-I, while chalcopyrite-II formed after sphalerite-I. Furthermore, the Cu ores contain galena (i) micro-veinlet aggregates that fill fractures within chalcopyrite, tetrahedrite and arsenopyrite; or (ii) granular forms that are enclosed by the late stage minerals (Fig. 5a-l). This means that in the Cu ores, galena-II formed after chalcopyrite-I. In addition, the chalcopyrite disease structure (Barton and Bethke, 1987) in sphalerite of the Pb-Zn ores (Fig. 4f) indicates that chalcopyrite-III formed simultaneously with sphalerite-III. Although the presence of low-angle contacts between sphalerite and galena/chalcopyrite in both the Pb-Zn and Cu ores may indicate a metasomatic or replacement association (Fig. 4b, j, l; Barton and Bethke, 1987; Frost et al., 2002; Tomkins et al., 2007), chalcopyrite has a much more obvious coeval paragenetic relationship to sphalerite and galena (Figs. 4 and 5). Hence, the Cu and Pb-Zn sulfides in Tianbaoshan appear to be co-genetic and were the products of different phases in an evolving hydrothermal system. This association of the Cu

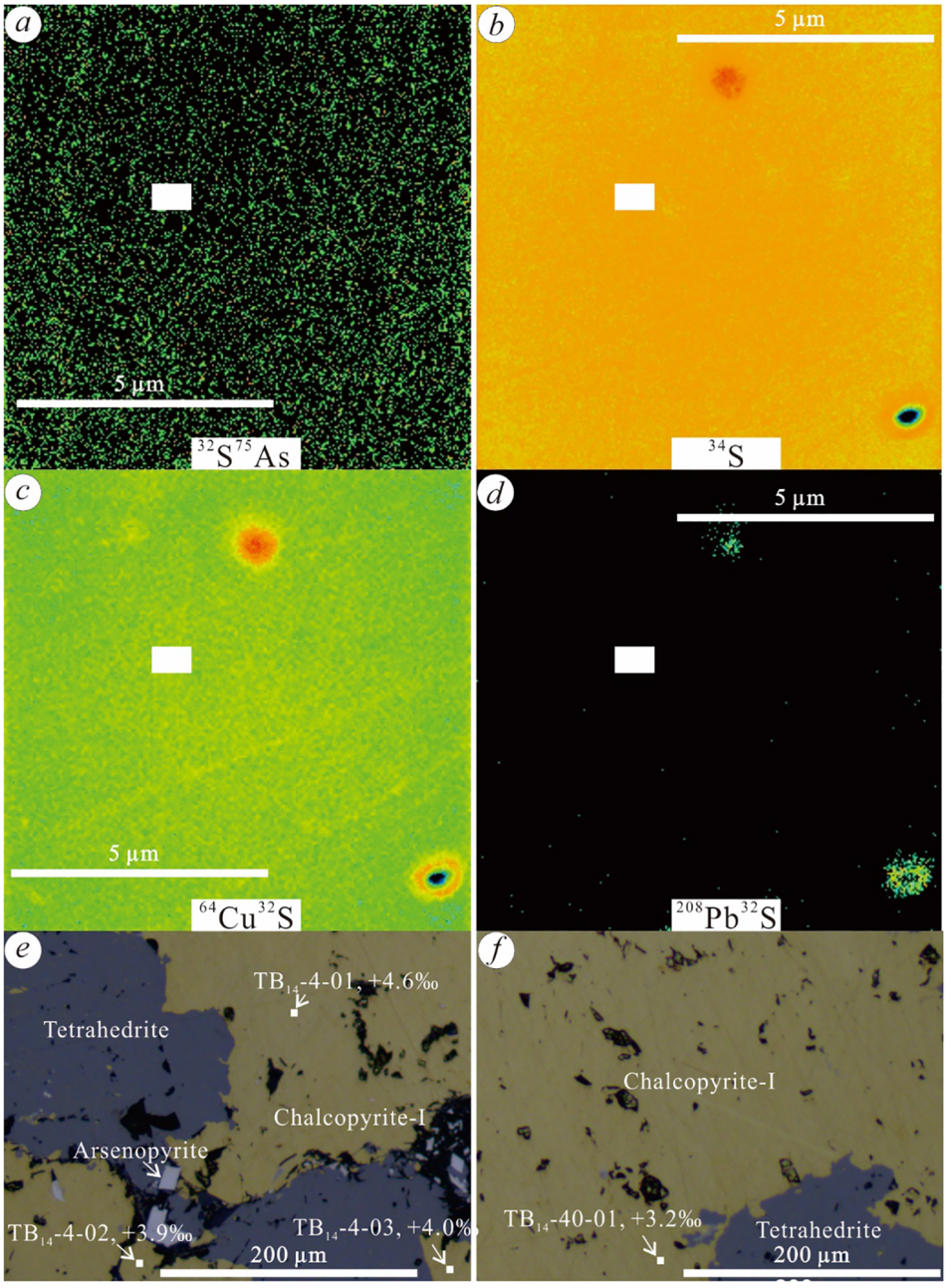

Fig. 6. (a-d) The best target areas selected for in-situ sulfur isotope analysis that have homogeneous isotopic compositions; (e-f) In-situ $\delta^{34}S$ values for chalcopyrite.

and Pb-Zn is different from that of MVT deposits in Missouri, USA (Burstein et al., 1993), the Wieloch deposit, Germany (Pfaff et al., 2009) and the Capricorn deposit, Australia (Muhling et al., 2012), which do not contain Cu sulfide ores.

Previous studies classified the Tianbaoshan deposit as a MVT deposit (Wang et al., 2000; Zhang et al., 2015). However, this deposit displays a set of features that differ from the typical MVT deposits. For example, sulfides precipitated from a Ca^{2+}-Mg^{2+}-Cl^{-}-HCO_3^{-} hydrothermal system with relatively high temperatures (Cu stage: 370–300 °C and Zn-Pb stage: 250–120 °C) and low salinities (< 10 wt% NaCl equiv.: Wang et al., 2000; Zhang, 2017) in Tianbaoshan. This is significantly different from typical MVT deposits that are related to basin brines (Leach et al., 2005, 2010), which are characterized by low temperatures (90–200 °C) and high salinities (> 10 wt% NaCl equiv.). In addition, the Tianbaoshan deposit has much higher ore grades (> 10 wt% Pb + Zn) than typical MVT deposits (< 10 wt% Pb + Zn). Only a few MVT deposits (such as the Viburnum Trend in the USA) are rich in Cu (Leach et al., 2005), but the Tianbaoshan deposit not only contains abundant Cu but also has discrete Cu ore bodies (Fig. 2b). Moreover, MVT deposits are not associated with igneous activities (e.g. Leach et al., 2010), whereas the Tianbaoshan Pb-Zn-(Cu) deposit has a spatial and genetic association with the ELIP. Furthermore, the Tianbaoshan deposit is structurally controlled by compressional tectonism as evidenced by the presence of reverse faults and folds (Figs. 1 and 2), whereas MVT deposits commonly occur along normal faults (Leach et al., 2005, 2010). Therefore, the Tianbaoshan deposit is not a typical MVT deposit, and represents a unique new type of epigenetic carbonate-hosted sulfide deposits in the Upper Yangtze province.

6.2. Sources of sulfur and metals

6.2.1. Sources of sulfur

All the main sulfide separates (pyrite, sphalerite and galena) from the Pb-Zn ores have bulk $\delta^{34}S$ values of −1.1–+7.3‰ (Wang et al.,

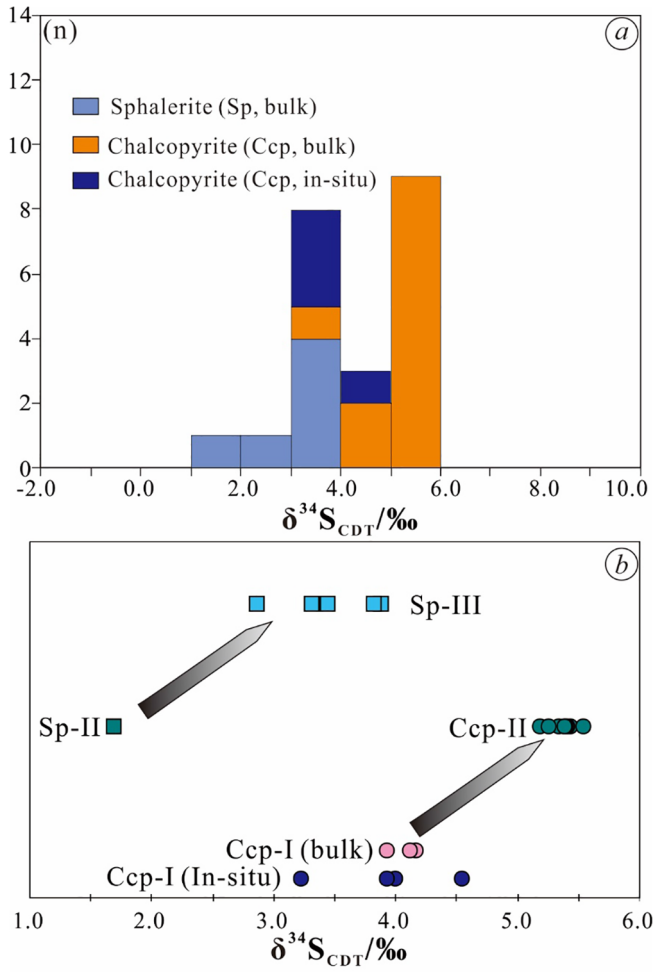

Fig. 7. (a) Histogram of sulfur isotopic compositions for the Tianbaoshan deposit; (b) Variation of sulfur isotopes from the early sulfide phases to the late ones.

2000; Zhou et al., 2013c; Sun et al., 2016; Zhu et al., 2016; Zhang, 2017; this study). Such sulfur isotope signatures suggest that the $\delta^{34}S_{\Sigma S\text{-}fluids}$ value was +4.7‰ or +4.2‰ (Wang et al., 2000; Zhu et al., 2016), on the basis of lack of sulfates. Our new in-situ and bulk $\delta^{34}S$ values of chalcopyrite-I and chalcopyrite-II range from +3.2 to +5.5‰ (Table 2; Figs. 6e-f and 7), which are similar to the $\delta^{34}S_{\Sigma S\text{-}fluids}$ value. As we have shown the Cu and Pb-Zn ores are co-genetic, so the source of sulfur for the Cu ores should be the same to that of the Pb-Zn ores. Three sources of sulfur have been proposed: (i) a mixed sulfur source of marine sulfate, which has undergone thermochemical sulfate reduction (TSR) and bacterial sulfate reduction (BSR) (Wang et al., 2000); (ii) a single sulfur source of evaporated marine sulfate by TSR (Zhou et al., 2013c); and (iii) a mixed sulfur source of magmatic sulfur, which was leached from Proterozoic basement volcanic rocks, and sedimentary sulfur (Zhu et al., 2016).

In Fig. 1b, the Proterozoic igneous rocks within the Tianbaoshan Formation (*ca.* 1 Ga; Geng et al., 2007) are much older than the Tianbaoshan deposit, and the Permian Emeishan flood basalts were also erupted (*ca.* 260 Ma; Zhou et al., 2002) prior to the sulfide mineralization. Those igneous rocks have $\delta^{34}S$ values of −3–+3‰ (Chaussidon et al., 1989; Seal, 2006; Zhu et al., 2016). Hence, we cannot preclude the possibility that reduced sulfur leached from these igneous rocks. On the other hand, it has been confirmed that TSR can produce a fractionation of +10–+20‰ between evaporated sulfates and sulfides in MVT hydrothermal systems (Claypool et al., 1980; Ohmoto et al., 1990; Machel et al., 1995; Worden et al., 1995; Ohmoto and Goldhaber, 1997). The evaporated marine sulfates within ore-hosting strata having $\delta^{34}S$ values of +20–+28‰ (Liu and Lin, 1999; Zhou et al., 2013b, 2014b). Hence, if the fractionation was +20‰ (Ohmoto et al., 1990), the resulting $\delta^{34}S$ values of sulfides would be 0–+8‰, which is in accord with the determined data (−1.1–+7.3‰). In contrast, the relatively high temperature of hydrothermal fluids (Cu stage: 370–300 °C and Pb-Zn stage: 250–120 °C; Wang et al., 2000; Zhang, 2017) exclude BSR, which is restricted to temperature of < 110 °C and could result in a larger sulfur isotope fractionation (up to +40‰; Jørgenson et al., 1992; Basuki et al., 2008). Therefore, a mixed sulfur source consisting of a magmatic sulfur component related to the nearby igneous rocks and a reduced sulfur component generated by TSR from evaporated sulfates can explain the observed sulfur isotopes (Table 2; Figs. 6e-f and 7a-b). Such a mixed sulfur source can also explain the increased $\delta^{34}S$ values through the paragenetic sequence (Fig. 7b), as sedimentary sulfur was gradually included with the magmatic sulfur (derived from igneous rocks). On the other hand, in TSR, a shift in temperatures can also produce higher $\delta^{34}S$ values of chalcopyrite than paragenetically related sphalerite (Fig. 7b) (Seal, 2006; Hoefs, 2009 and references therein).

6.2.2. *Sources of metals*

The geological records suggests that the ~156–166 Ma (Zhang, 2017) diabase dykes post-date sulfide mineralization (Fig. 1c and 2a-b), so the formation age of the Tianbaoshan deposit should be older than 156–166 Ma. In addition, tectonic analyses (Zhang et al., 2006) and geochronological studies (Li et al., 2007; Zhou et al., 2013a, 2013b, 2015; Zhang et al., 2015; Hu et al., 2017) suggest that the carbonate-hosted Pb-Zn deposits in the Upper Yangtze province were formed during the Early Mesozoic (230–200 Ma). Hence, 200 Ma was used to correct the initial Pb isotopic ratios of potential source rocks is suitable (Carr et al., 1995; Muchez et al., 2005; Pass et al., 2014; Zhou et al., 2018a).

The chalcopyrite and galena crystals have similar in-situ Pb isotopic ratios determined by LA-MC-ICPMS that display a narrow range and high μ values (9.7–9.8) (Table 3; Fig. 8). Chalcopyrite and galena of different ore formation phases are characterized by higher $^{207}Pb/^{204}Pb$ ratios at given $^{206}Pb/^{204}Pb$ ratios comparable to the ore-forming age-corrected (200 Ma) Proterozoic basement metamorphic rocks (Fig. 8). Their $^{207}Pb/^{204}Pb$ ratios are also significantly higher than those of the age-corrected (200 Ma) late Permian continental flood basalts of the ELIP, plotting above the Pb evolution curve of upper continental crust (Fig. 8). In addition, the $^{206}Pb/^{204}Pb$ ratios of these chalcopyrite and galena crystals are slightly more radiogenic than those of the age-corrected (200 Ma) host carbonate rocks of the Dengying Formation at given $^{207}Pb/^{204}Pb$ ratios (Fig. 8). These Pb isotope characteristics suggest a well-mixed source of Pb, and the mineralizing elements of both the Cu and Pb-Zn ores were related to basement rocks and sedimentary rocks, and even basalts, as suggested by geological records (Figs. 1b-c and 2a-b) and S isotopes (Figs. 6 and 7). Furthermore, the gradual increase in Pb isotopic ratios from the early to late stage precipitated sulfides (Fig. 9) further suggests that the sedimentary rocks with high Pb isotopic ratios contribute more metal Pb to the hydrothermal fluids at the late stage than the early stage along.

6.3. *Implications for the regional metallogeny*

There are > 400 Pb-Zn deposits in the Upper Yangtze province, so why has such a significant Cu mineralization occurred at Tianbaoshan? We considered that the local geological setting determined the combination of mineralizing elements. For example, the exposed Proterozoic basement rocks in Tianbaoshan (Figs. 1 and 2) contain sulfur-rich igneous rocks and have high Cu-Pb-Zn background values (e.g. Wang et al., 2000), which are considered to be the crucial sources of mineralizing elements (sulfur and metals; Zhu et al., 2016; Bao et al., 2017; Zhou et al., 2018a). In addition, the nearby basalts of the ELIP are also

Table 3
Femtosecond (fs) LA-MC-ICPMS in situ Pb isotopic ratios of the Tianbaoshan Pb-Zn-(Cu) deposit, South China.

No.	Location	Mineral	$^{206}Pb/^{204}Pb$	1 s	$^{207}Pb/^{204}Pb$	1 s	$^{208}Pb/^{204}Pb$	1 s	μ
TB_{14}-27-01	2036m	Ccp-I	18.453	0.002	15.740	0.002	38.840	0.005	9.74
TB_{14}-27-02	2036m	Ccp-II	18.465	0.004	15.752	0.004	38.865	0.010	9.76
TB_{14}-27-03	2036m	Ccp-I	18.442	0.005	15.732	0.005	38.809	0.013	9.72
TB_{14}-27-04	2036m	Ccp-I	18.452	0.007	15.738	0.006	38.827	0.014	9.73
TB_{14}-27-05	2036m	Ccp-I	18.447	0.007	15.732	0.006	38.812	0.015	9.72
TB_{14}-27-06	2036m	Ccp-I	18.445	0.006	15.730	0.005	38.809	0.014	9.72
TB_{14}-27-07	2036m	Ccp-I	18.458	0.004	15.745	0.003	38.852	0.008	9.74
TB_{14}-27-08	2036m	Ccp-I	18.454	0.002	15.741	0.002	38.836	0.004	9.74
TB_{14}-27-09	2036m	Ccp-I	18.455	0.001	15.743	0.001	38.846	0.004	9.74
TB_{14}-27-10	2036m	Ccp-I	18.446	0.002	15.732	0.002	38.808	0.005	9.72
TB_{14}-27-11	2036m	Ccp-I	18.455	0.002	15.744	0.002	38.851	0.006	9.74
TB_{14}-27-12	2036m	Ccp-I	18.444	0.004	15.730	0.003	38.816	0.009	9.72
TB_{14}-27-13	2036m	Ccp-I	18.450	0.001	15.737	0.001	38.828	0.004	9.73
TB_{14}-27-14	2036m	Ccp-I	18.453	0.003	15.741	0.003	38.838	0.007	9.74
TB_{14}-27-15	2036m	Ccp-I	18.431	0.008	15.715	0.007	38.780	0.018	9.69
TB_{14}-27-16	2036m	Ccp-II	18.467	0.002	15.755	0.002	38.878	0.005	9.76
TB_{14}-34-01	2064m	Ccp-II	18.473	0.001	15.741	0.001	38.868	0.004	9.73
TB_{14}-34-02	2064m	Ccp-II	18.476	0.001	15.742	0.001	38.874	0.004	9.74
TB_{14}-34-03	2064m	Ccp-II	18.476	0.001	15.741	0.001	38.872	0.003	9.74
TB_{14}-34-04	2064m	Ccp-II	18.477	0.002	15.742	0.002	38.876	0.005	9.74
TB_{14}-34-05	2064m	Ccp-II	18.477	0.001	15.742	0.001	38.874	0.003	9.74
TB_{14}-34-06	2064m	Ccp-II	18.474	0.001	15.739	0.001	38.868	0.004	9.73
TB_{14}-34-07	2064m	Ccp-II	18.482	0.002	15.747	0.002	38.892	0.006	9.75
TB_{14}-34-08	2064m	Ccp-II	18.477	0.001	15.745	0.002	38.879	0.005	9.74
TB_{14}-34-09	2064m	Ccp-II	18.470	0.001	15.740	0.001	38.863	0.004	9.73
TB_{14}-34-10	2064m	Ccp-II	18.470	0.001	15.740	0.001	38.862	0.004	9.73
TB_{14}-34-11	2064m	Ccp-II	18.480	0.002	15.753	0.002	38.894	0.007	9.76
TB_{14}-34-12	2064m	Ccp-II	18.475	0.002	15.745	0.002	38.874	0.006	9.74
TB_{14}-34-13	2064m	Ccp-II	18.474	0.001	15.743	0.002	38.867	0.005	9.74
TB_{14}-34-14	2064m	Ccp-I	18.465	0.002	15.736	0.002	38.844	0.005	9.73
TB_{14}-34-15	2064m	Ccp-II	18.469	0.003	15.740	0.003	38.860	0.007	9.73
TB_{14}-34-16	2064m	Ccp-II	18.468	0.002	15.740	0.002	38.856	0.006	9.73
TB_{14}-6-01	2044m	Gal-II	18.474	0.003	15.759	0.003	38.886	0.008	9.77
TB_{14}-6-02	2044m	Gal-I	18.445	0.002	15.749	0.002	38.835	0.005	9.75
TB_{14}-6-03	2044m	Gal-II	18.466	0.002	15.760	0.002	38.888	0.006	9.77
TB_{14}-6-04	2044m	Gal-II	18.469	0.002	15.753	0.002	38.880	0.006	9.76
TB_{14}-6-05	2044m	Gal-III	18.482	0.003	15.761	0.003	38.914	0.008	9.77
TB_{14}-6-06	2044m	Gal-III	18.482	0.003	15.764	0.003	38.931	0.007	9.78
TB_{14}-6-07	2044m	Gal-II	18.472	0.002	15.755	0.002	38.897	0.006	9.76
TB_{14}-6-08	2044m	Gal-III	18.477	0.002	15.759	0.002	38.919	0.007	9.77
TB_{14}-6-09	2044m	Gal-II	18.468	0.002	15.753	0.002	38.876	0.006	9.76
TB_{14}-6-10	2044m	Gal-III	18.479	0.003	15.761	0.003	38.910	0.008	9.77
TB_{14}-6-11	2044m	Gal-III	18.481	0.003	15.763	0.003	38.922	0.007	9.78
TB_{14}-6-12	2044m	Gal-III	18.482	0.003	15.762	0.003	38.909	0.007	9.78
TB_{14}-6-13	2044m	Gal-II	18.475	0.003	15.755	0.003	38.873	0.007	9.76
TB_{14}-6-14	2044m	Gal-II	18.479	0.003	15.761	0.003	38.884	0.008	9.77
TB_{14}-6-15	2044m	Gal-II	18.470	0.003	15.755	0.003	38.872	0.007	9.76
TB_{14}-6-16	2044m	Gal-III	18.482	0.003	15.765	0.003	38.912	0.009	9.78
TB_{14}-30-01	2064m	Gal-I	18.442	0.003	15.747	0.003	38.793	0.007	9.75
TB_{14}-30-02	2064m	Gal-I	18.445	0.002	15.748	0.002	38.790	0.006	9.75
TB_{14}-30-03	2064m	Gal-I	18.452	0.003	15.752	0.003	38.808	0.008	9.76
TB_{14}-30-04	2064m	Gal-I	18.445	0.003	15.746	0.003	38.793	0.007	9.75
TB_{14}-30-05	2064m	Gal-I	18.448	0.003	15.747	0.003	38.795	0.007	9.75
TB_{14}-30-06	2064m	Gal-I	18.441	0.002	15.741	0.002	38.774	0.006	9.74
TB_{14}-30-07	2064m	Gal-I	18.447	0.002	15.748	0.002	38.793	0.006	9.75
TB_{14}-30-08	2064m	Gal-I	18.442	0.002	15.747	0.002	38.792	0.006	9.75
TB_{14}-30-09	2064m	Gal-II	18.470	0.002	15.755	0.002	38.883	0.006	9.76
TB_{14}-30-10	2064m	Gal-III	18.480	0.003	15.763	0.003	38.917	0.008	9.78
TB_{14}-30-11	2064m	Gal-III	18.482	0.003	15.765	0.003	38.929	0.007	9.78
TB_{14}-30-12	2064m	Gal-III	18.484	0.003	15.764	0.003	38.916	0.007	9.78
TB_{14}-30-13	2064m	Gal-II	18.477	0.003	15.757	0.003	38.880	0.007	9.77
TB_{14}-30-14	2064m	Gal-II	18.481	0.003	15.763	0.003	38.891	0.008	9.78
TB_{14}-30-15	2064m	Gal-II	18.472	0.003	15.757	0.003	38.879	0.007	9.77
TB_{14}-30-16	2064m	Gal-III	18.483	0.003	15.767	0.003	38.919	0.009	9.79

Ccp-chalcopyrite; Gnal-galena. $\mu = {}^{238}U/{}^{204}Pb$.

the possible sources of sulfur and metals, as evidenced by in situ S-Pb isotopes (Figs. 6–9). Furthermore, some deposits in the Upper Yangtze province close to the basement rocks and basalts are rich in Cu, and even appear Cu and Ni minerals, for example the Fule deposit (Zhou et al., 2018b). In contrast, some deposits far from the basement and basalts contain rare Cu, such as the Nayongzhi deposit (Zhou et al., 2018c).

We interpret the regional Pb-Zn-(Cu) metallogeny as follows: (i) The geothermal gradients in the western margin of the Yangtze Block, South China were elevated by underplating and eruption of the Permian flood basalts of the EILP through heating (Zhou et al., 2018a). This event provided fluids and heat that caused the extraction of ore-forming elements from Proterozoic basement rocks and Paleozoic sedimentary rocks, and then resulted in the formation of hot and cold mineralizing

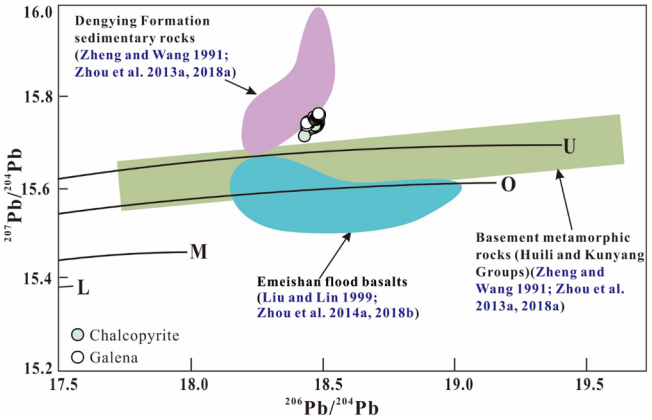

Fig. 8. Plot of $^{207}Pb/^{204}Pb$ vs. $^{206}Pb/^{204}Pb$. Trends for the Upper Crust (U), Orogenic Belt (O), Mantle (M) and Lower Crust (L) are from Zartman and Doe (1981). Whole-rock Pb isotopic ratios are ore formation age-corrected at 200 Ma.

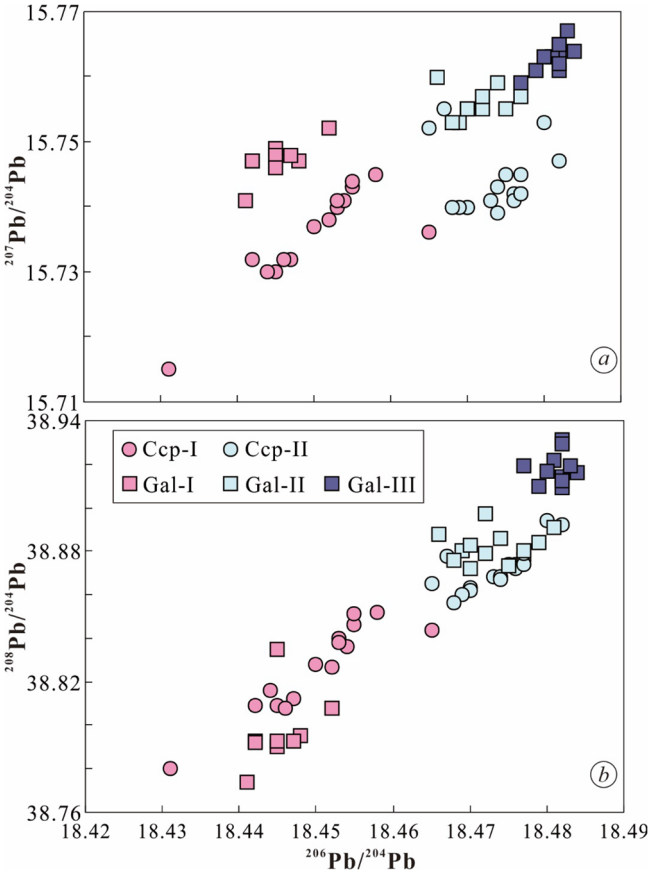

Fig. 9. Variation of Pb isotopes from the early sulfide phases to the late ones in the plots of $^{207}Pb/^{204}Pb$ vs. $^{206}Pb/^{204}Pb$ (a) and $^{208}Pb/^{204}Pb$ vs. $^{206}Pb/^{204}Pb$ (b).

fluids, respectively. (ii) After eruption of the Permian Emeishan basalts, the western Yangtze Block collided with adjacent blocks (such as Yidun Arc) and caused the closure of the Paleo-Tethys Ocean (Zhang et al., 2006; Reid et al., 2007; Hu and Zhou, 2012). Such an Indosinian Orogeny provided a tectonic dynamic source for the migration of these fluids. (iii) During the Early Mesozoic (230–200 Ma), the tectonic regime in the Upper Yangtze province shifted from compression to extension (Zhang et al., 2006; Qiu et al., 2016; Faure et al., 2017; Zhou et al., 2018a), causing the excretion of these fluids along the regional structures, such as the Anninghe and Xiaojiang faults (Fig. 1b). The mixing of hot and cold fluids resulted in the rapid precipitation of the early stage sulfides and the generation of reduced sulfur by TSR, and then the extraction of partial ore-forming elements from the local rocks (such as the Dengying Formation sedimentary rocks) through W/R (water/rock) interaction (Fig. 9). During deposition, the Cu ores would precipitate firstly, followed by the Pb-Zn ores. The sulfide rapid precipitation or a shift in temperatures of TSR is responsible for the variation of sulfur isotopes (Figs. 6 and 7).

7. Conclusions

(1) Sulfur isotopes imply reduced sulfur was derived from a mixed source of magmatic sulfur (derived from igneous rocks) and evaporated marine sulfate by TSR, and the variation of sulfur isotopes results from either incorporation of different proportions of these sources or a shift in temperatures of TSR.
(2) Lead isotopes suggest that both the Cu and Pb-Zn ores have the same sources of metals and the variation of Pb isotopes indicates a more radiogenic source (such as the Dengying Formation sedimentary rocks) may be involved during the late stage.
(3) Both the Cu and Pb-Zn ores are co-genetic and they formed from an evolving hydrothermal system that is related to the Emeishan large igneous province and Indosinian Orogeny.
(4) The Tianbaoshan Pb-Zn-(Cu) deposit is interpreted as a new type of carbonate-hosted epigenetic sulfide deposit, which has many characteristics that are different from those of the typical MVT deposits.

Acknowledgements

We thank Profs. Han-Jie Wen, Xuan-Ce Wang and Simon A. Wilde for useful discussion. Comments and suggestions from Profs. Carr Graham, David Huston and Franco Pirajno (Editor-in-Chief), and anonymous reviewers significantly improved the quality of this paper. This research was financially supported by the National Natural Science Foundation of China (41872095), the National Key R&D Project of China (2017YFC0602502), the Key Project of National Natural Science Foundation of China (41430315), and the Talent Introduction (YJRC4201804) and Cultivation Projects (2018YDJQ009) of Yunnan University to J.X Zhou.

Appendix A

Bulk S isotope analysis

Powders of sulfide separates (< 200 mesh) were mixed with copper oxide (CuO) powder, and then heated to extract SO_2 gas. Sulfur isotopic compositions of the extracted SO_2 were determined at the State Key Laboratory of Environmental Geochemistry, Institute of Geochemistry, Chinese Academy of Sciences, using a Finnigan MAT-251 mass spectrometer. The $^{34}S/^{32}S$ ratios are expressed by the conventional $\delta^{34}S$ value in per mil relative to the Vienna Canyon Diablo Troilite (V-CDT) standard. GBW 04,414 ($\delta^{34}S = -0.07 \pm 0.12‰$) and GBW 04,415 ($\delta^{34}S = +22.14 \pm 0.15‰$) Ag_2S were used as the external standards. The analytical uncertainty was ± 0.2‰ (2σ).

In-situ S isotope analysis

In-situ S isotope analysis was performed at the Key Laboratory of Earth and Planetary Physics, Institute of Geology and Geophysics, Chinese Academy of Sciences, using a CAMECA NanoSIMS. The measurements were made using 3 different settings of the Faraday cups/electron multiplier (EM) detectors, for meeting the diverse requirements of spatial resolution. The bracketing method of standard-sample-standard was applied to correct for instrumental mass fractionation. Target spots of the most homogeneous isotopes (e.g. ^{32}S, ^{34}S and ^{63}Cu in

Fig. 6a-d) were selected for determining the most credible sulfur isotopic data. International standards included Balmat and CAR 123, and internal standards included CPY-1117 (chalcopyrite). The analytical precision calculated from replicate analyses of the unknown samples was better than 0.2‰ (1σ). The in-situ S isotopic compositions were reported relative to the Vienna Canyon Diablo Troilite (V-CDT) standard. Details of NanoSIMS in-situ S isotope analysis techniques and instrument parameters were described in Zhang et al. (2014) and Zhou et al. (2018b, 2018c).

In-situ Pb isotope analysis

In-situ Pb isotope analysis was carried out using a Nu II MC-ICP-MS instrument (Nu Instruments, Wrexham, UK) combined with a 266 nm NWR UP Femto laser ablation system (ESI, USA) at the State Key Laboratory of Continental Dynamics, Northwest University. Prior to analysis, surface of sulfides was cleaned with Milli-Q (18.2MΩ·cm) pure water using cotton bud to remove any contamination. Line scan ablation consisted of background collection for 20 s followed by 50 s of laser ablation for signal collection. Laser ablation parameters include spot size of 15 μm for galena and 50 μm for chalcopyrite, 100% output energy of > 600 μJ, 100% energy density of 6 J/cm^2, laser frequency of 5–50 Hz, and ablation way of line 3 μm/s. A strong enough Pb signal was possible for analyses of sulfide samples. The Tl (20 ppb, NIST SRM 997, $^{205}Tl/^{203}Tl = 2.38890$) and NIST SRM 610 glass were served as internal and external standards, respectively. The repeated analyses of NIST SRM 610 glass standard yielded highly reliable and reproducible results during the whole analytical process with mean $^{206}Pb/^{204}Pb$, $^{207}Pb/^{204}Pb$ and $^{208}Pb/^{204}Pb$ ratios of 17.052 ± 0.003, 15.515 ± 0.003 and 36.980 ± 0.007 (1 s, $n = 183$), respectively. The details of LA-MC-ICPMS in-situ Pb isotope analysis and instrument parameters were described in Bao et al. (2016, 2017) and Zhou et al. (2018b).

References

Bao, Z., Yuan, W., Yuan, H., Liu, X., Chen, K., Zong, C., 2016. Non-matrix-matched determination of lead isotope ratios in ancient bronze artifacts by femtosecond laser ablation multi-collector inductively coupled plasma mass spectrometry. Inter. J. Mass Spectrom. 402, 12–19.

Bao, Z., Li, Q., Wang, C.Y., 2017. Metal source of giant Huize Zn-Pb deposit in SW China: New constraints from in situ Pb isotopic compositions of galena. Ore Geol. Rev. 91, 824–836.

Barton, J.P.B., Bethke, P.M., 1987. Chalcopyrite disease in sphalerite: pathology and epidemiology. Amer. Mineral. 72, 451–467.

Basuki, N.I., Taylor, B.E., Spooner, E.T.C., 2008. Sulfur isotope evidence for thermochemical reduction of dissolved sulfate in Mississippi valley type zinc-lead mineralization, Bongara area, northern Peru. Econ. Geol. 103, 83–799.

Burstein, I.B., Shelton, K.L., Gregg, J.M., Hagni, R.D., 1993. Complex, multiple ore fluids in the world class Southeast Missouri Pb-Zn-Cu MVT deposits: Sulfur isotope evidence. Conference: 27 annual Geological Society of America (GSA) North-Central Section meeting, Rolla, MO (United States), Mar 29-30, Abstracts with Programs, 25, 3 (CONF-9303210).

Carr, G.R., Dean, J.A., Suppel, D.W., Heithersay, P.S., 1995. Precise lead isotope fingerprinting of hydrothermal activity associated with Ordovician to Carboniferous metallogenic events in the Lachlan fold belt of New South Wales. Econ. Geol. 90, 1467–1505.

Chaussidon, M., Albarède, F., Sheppard, S.M.F., 1989. Sulphur isotope variations in the mantle from ion microprobe analyses of micro-sulphide inclusions. Earth Planet. Sci. Lett. 92, 144–156.

Chen, K.Y., Yuan, H.L., Bao, Z.A., Zong, C.L., Dai, M.N., 2014. Precise and accurate in situ determination of lead isotope ratios in NIST, USGS, MPI-DING and CGSG glass reference materials using femtosecond laser ablation MC-ICP-MS. Geostand. Geoanal. Res. 38, 5–21.

Cromie, P.W., Gosse, R.R., Zhang, P., Zhu, X., 1996. Exploration for carbonate-hosted Pb-Zn deposits. Sichuan, P.R.C. [abs.]: International Geological Congress, 30th, Beijing, China. Abstracts, 412.

Claypool, G.E., Holser, W.T., Kaplan, I.R., Sakai, H., Zak, I., 1980. The age curves of sulfur and oxygen isotopes in marine sulfate and their mutual interpretation. Chem. Geol. 28, 199–260.

Faure, M., Chen, Y., Feng, Z., Shu, L., Xu, Z., 2017. Tectonics and geodynamics of South China: An introductory note. J. Asian Earth Sci. 141, 1–6.

Frost, B.R., Mavrogenes, J.A., Tompkins, A., 2002. Partial melting of sulfide ore deposits during medium and high-grade metamorphism. Canadian Mineral. 40, 1–18.

Geng, Y.S., Yang, C.H., Du, L.L., Wang, X.S., Ren, L.D., Zhou, X.W., 2007. Chronology and tectonic environment of the Tianbaoshan Formation: New evidence from zircon SHRIMP U-Pb age and geochemistry. Geol. Rev. 53, 556–563 (in Chinese with English abstract).

Hoefs, J., 2009. Stable isotope geochemistry, sixth ed. Springer-Verlag Berlin Heidelberg doi: 10.1007/978-3-540-70708-0.

Hu, R.Z., Zhou, M.F., 2012. Multiple Mesozoic mineralization events in South China-an introduction to the thematic issue. Miner. Deposita 47, 579–588.

Hu, R., Fu, S., Huang, Y., Zhou, M., Fu, S., Zhao, C., Wang, Y., Bi, X., Xiao, J., 2017. The giant South China Mesozoic low-temperature metallogenic domain: Reviews and a new geodynamic model. J. Asian Earth Sci. 137, 9–34.

Huang, Z., Li, X., Zhou, M., Li, W., Jin, Z., 2010. REE and C-O isotopic geochemistry of calcites from the word–class Huize Pb-Zn deposits, Yunnan, China: implication for the ore genesis. Acta Geol. Sinica 84, 597–613.

Ikehata, K., Notsu, K., Hirata, T., 2008. In situ determination of Cu isotope ratios in copper-rich materials by NIR femtosecond LA-MC-ICP-MS. J. Anal. Atom. Spectrom. 23, 1003–1008.

Jin, Z.G., Zhou, J.X., Huang, Z.L., Ye, L., Luo, K., Gao, J.G., Chen, X.L., Wang, B., Peng, S., 2016. Ore genesis of the Nayongzhi Pb-Zn deposit, Puding city, Guizhou Province, China: Evidences from S and in situ Pb isotopes. Acta Petrol. Sinica 32, 3441–3455 (in Chinese with English abstract).

Jørgenson, B.B., Isaksen, M.F., Jannasch, H.W., 1992. Bacterial sulfate reduction above 100°C in deep sea hydrothermal vent sediments. Science 258, 1756–2175.

LaFlamme, C., Martin, L., Jeon, H., Reddy, S.M., Selvaraja, V., Caruso, S., Bui, T.H., Roberts, M.P., Voute, F., Hagemann, S., Wacey, D., Littman, S., Wing, B., Fiorentini, M., Kilburn, M.R., 2016. In situ multiple sulfur isotope analysis by SIMS of pyrite, chalcopyrite, pyrrhotite, and pentlandite to refine magmatic ore genetic models. Chem. Geol. 444, 1–15.

Leach, D.L., Sangster, D., Kelley, K.D., Large, R.R., Garven, G., Allen, C., Gutzmer, J., Walters, S., 2005. Sediment-hosted lead-zinc deposits: A global perspective. Econ. Geol. 100th Anniversary Volume, 561–607.

Leach, D.L., Bradley, D.C., Huston, D., Pisarevsky, S.A., Taylor, R.D., Gardoll, S.J., 2010. Sediment-hosted lead-zinc deposits in Earth history. Econ. Geol. 105, 593–625.

Li, B., Zhou, J.X., Huang, Z.L., Yan, Z.F., Bao, G.P., Sun, H.R., 2015. Geological, rare earth elemental and isotopic constraints on the origin of the Banbanqiao Zn–Pb deposit, southwest China. J. Asian Earth Sci. 111, 100–112.

Li, H., Zhang, Z., Santosh, M., Lv, L., Han, L., Liu, W., 2017. Late Permian basalts in the Yanghe area, eastern Sichuan Province, SW China: Implications for the geodynamic of the Emeishan flood basalts province and Permian global mass extinction. J. Asian Earth Sci. 134, 293–308.

Li, W.B., Huang, Z.L., Yin, M.D., 2007. Dating of the giant Huize Zn-Pb ore field of Yunnan province, southwest China: Constraints from the Sm-Nd system in hydrothermal calcite. Resource Geol. 57, 90–97.

Liu, H.C., Lin, W.D., 1999. Study on the law of Pb-Zn-Ag ore deposit in northeast Yunnan, China. Yunnan Univ Press, Kunming, pp. 1–468 (in Chinese).

Machel, H.G., Krouse, H.R., Sassen, R., 1995. Products and distinguishing criteria of bacterial and thermo-chemical sulfate reduction. Appl. Geochem. 10, 373–389.

Muchez, P., Heijlen, W., Banks, D., Blundell, D., Boni, M., Grandia, F., 2005. Extensional tectonics and the timing and formation of basin-hosted deposits in Europe. Ore Geol. Rev. 27, 241–267.

Muhling, J.R., Fletcher, I.R., Rasmussen, B., 2012. Dating fluid flow and Mississippi Valley type base-metal mineralization in the Paleoproterozoic Earaheedy Basin, Western Australia. Precambrian Res. 212, 75–90.

Ohmoto, H., Goldhaber, M.B., 1997. Sulfur and carbon isotopes. In: Barnes, H.L. (Ed.), Geochemistry of hydrothermal ore deposits, 3rd ed. Wiley, New York, pp. 517–611.

Ohmoto, H., Kaiser, C.J., Geer, K.A., 1990. Systematic of sulfur isotopes in recent marine sediments and ancient sediment–hosted base metal deposits In H. K Herbert and S. E. Ho (Editors), Stable isotopes and Fluid Processes in Mineralization. Geol. Dep Univ. Extens. Univ. Western Australia 23, 70–120.

Pass, H.E., Cookem, D.R., Davidson, G., Maas, R., Dipple, G., Rees, C., Ferreira, L., Taylor, C., Deyell, C.L., 2014. Isotope geochemistry of the northeast zone, Mount Polley alkalic Cu-Au-Ag porphyry deposit, British Columbia: A case for carbonate assimilation. Econ. Geol. 109, 859–890.

Pfaff, K., Wagner, T., Markl, G., 2009. Fluid mixing recorded by mineral assemblage and mineral chemistry in a Mississippi Valley-type Pb-Zn-Ag deposit in Wiesloch, SW Germany. J. Geochem. Explor. 101, 81.

Qiu, L., Tang, S.L., Wang, Q., Yang, W.X., Tang, X.L., Wang, J.B., 2016. Mesozoic geology of southwestern China: Indosinian foreland overthrusting and subsequent deformation. J. Asian Earth Sci. 122, 91–105.

Reid, A., Wilson, C.J.L., Shun, L., Pearson, N., Belousova, E., 2007. Mesozoic plutons of the Yidun Arc, SW China: U-Pb geochronology and Hf isotopic signature. Ore Geol. Rev. 31, 88–106.

Seal, I.R., 2006. Sulfur isotope geochemistry of sulfide minerals. Rev. Miner. Geochem. 61, 633–677.

Sun, W.H., Zhou, M.F., Gao, G.F., Yang, Y.H., Zhao, X.F., Zhao, J.H., 2009. Detrital zircon U-Pb geochronological and Lu-Hf isotopic constraints on the Precambrian magmatic and crustal evolution of the western Yangtze Block, SW China. Precambrian Res. 172, 99–126.

Sun, H.R., Zhou, J.X., Huang, Z.L., Fan, H.F., Ye, L., Luo, K., Gao, J.G., 2016. The genetic relationship between Cu and Zn dominant mineralization in the Tianbaoshan deposit, Southwest China. Acta Petrol. Sin. 32 (11), 3407–3417.

Tan, S.C., Zhou, J.X., Li, B., Zhao, J.X., 2017. In situ Pb and bulk Sr isotope analysis of the Yinchanggou Pb-Zn deposit in Sichuan Province (SW China): Constraints on the origin and evolution of hydrothermal fluids. Ore Geol. Rev. 91, 432–443.

Tomkins, A.G., Pattison, D.R.M., Frost, B.R., 2007. On the initiation of metamorphic sulfide anatexis. J. Petrol. 48, 511–535.

Ushikubo, T., Williford, K.H., Farquhar, J., Johnston, D.T., Kranendonk, M.J.V., Valley, J.W., 2014. Development of in situ sulfur four-isotope analysis with multiple Faraday

cup detectors by SIMS and application to pyrite grains in a Paleoproterozoic glaciogenic sandstone. Chem. Geol. 383, 86–99.
Wang, X.C., Zheng, Z.R., Zheng, M.H., Xu, X.H., 2000. Metallogenic mechanism of the Tianbaoshan Pb-Zn deposit, Sichuan. Chin. J. Geochem. 19, 121–133.
Wang, C.M., Deng, J., Carranza, E.J.M., Lei, X.R., 2014. Nature, diversity and temporal-spatial distributions of sediment-hosted Pb-Zn deposit in China. Ore Geol. Rev. 56, 327–351.
Wang, L.J., Mi, M., Zhou, J.X., Luo, K., 2018. New constraints on the origin of the Maozu carbonate-hosted epigenetic Zn-Pb deposit in NE Yunnan Province, SW China. Ore Geol. Rev. 101, 578–594.
Whitney, D.L., Evans, B.W., 2010. Abbreviations for names of rock-forming minerals. Amer. Mineral. 95, 185–187.
Wu, T., Zhou, J.X., Wang, X.C., Li, W.X., Wilde, S.A., Sun, H.R., Wang, J.S., Li, Z., 2018. Identification of ca. 850 Ma high-temperature strongly peraluminous granitoids in southeastern Guizhou Province, South China: A result of early extension along the southern margin of the Yangtze Block. Precambrian Res. 308, 18–34.
Worden, R.H., Smalley, P.C., Oxtoby, N.H., 1995. Gas souring by the thermo chemical sulfate reduction at 140°C. AAPG Bull. 79, 854–863.
Xu, Y., Huang, Z., Zhu, D., Luo, T., 2014. Origin of hydrothermal deposits related to the Emeishan magmatism. Ore Geol. Rev. 63, 1–8.
Yuan, H.L., Yin, C., Liu, X., Chen, K.Y., Bao, Z.A., Zong, C.L., Dai, M.N., Lai, S.C., Wang, R., Jiang, S.Y., 2015. High precision in-situ Pb isotopic analysis of sulfide minerals by femtosecond laser ablation multi-collector inductively coupled plasma mass spectrometry. Sci. China.-Earth Sci. 58, 1713–1721.
Zartman, R.E., Doe, B.R., 1981. Plumbotectonics-the model. Tectonophysics 75, 135–162.
Zhang, F., 2017. Study on ore genesis of the Tianbaoshan Pb-Zn deposit and the regional metallogenetic geodynamical setting (Master Dissertation). China University of Geosciences (Beijing), pp. 1–82 (in Chinese with English abstract).
Zhang, Z.B., Li, C.Y., Tu, G.C., Xia, B., Wei, Z.Q., 2006. Geotectonic evolution background and ore-forming process of Pb-Zn deposits in Chuan-Dian-Qian area of southwest China. Geotec. Metall. 30, 343–354 (in Chinese with English abstract).
Zhang, J., Lin, Y., Yang, W., Shen, W., Hao, J., Hu, S., Cao, M., 2014. Improved precision and spatial resolution of sulfur isotope analysis using NanoSIMS. J. Anal. Atom. Spectrom. 29 (10), 1934–1943.
Zhang, C.Q., Wu, Y., Hou, L., Mao, J.W., 2015. Geodynamic setting of mineralization of Mississippi Valley-type deposits in world-class Sichuan-Yunnan-Guizhou Zn-Pb triangle, southwest China: Implications from age-dating studies in the past decade and the Sm-Nd age of the Jinshachang deposit. J. Asian Earth Sci. 103, 103–114.
Zhao, X.F., Zhou, M.F., Li, J.W., Sun, M., Gao, J.F., Sun, W.H., Yang, J.H., 2010. Late Paleoproterozoic to early Mesoproterozoic Dongchuan Group in Yunnan, SW China: Implications for tectonic evolution of the Yangtze Block. Precambrian Res. 182, 57–69.
Zheng, M.H., Wang, X.C., 1991. Genesis of the Daliangzi Pb-Zn deposit in Sichuan, China. Econ. Geol. 86, 831–846.
Zhou, C.X., Wei, C.S., Guo, J.Y., 2001. The source of metals in the Qilingchang Pb-Zn deposit, Northeastern Yunnan, China: Pb-Sr isotope constraints. Econ. Geol. 96, 583–598.
Zhou, J., Huang, Z., Zhou, G., Li, X., Ding, W., Bao, G., 2011. Trace elements and rare earth elements of sulfide minerals in the Tianqiao Pb-Zn ore deposit, Guizhou Province. China. Acta Geol. Sinica 85, 189–199.
Zhou, J., Huang, Z., Zhou, M., Li, X., Jin, Z., 2013a. Constraints of C-O-S-Pb isotope compositions and Rb-Sr isotopic age on the origin of the Tianqiao carbonate-hosted Pb-Zn deposit, SW China. Ore Geol. Rev. 53, 77–92.
Zhou, J., Huang, Z., Yan, Z., 2013b. The origin of the Maozu carbonate-hosted Pb-Zn deposit, southwest China: Constrained by C-O-S-Pb isotopic compositions and Sm-Nd isotopic age. J. Asian Earth Sci. 73, 39–47.
Zhou, J., Gao, J., Chen, D., Liu, X., 2013c. Ore genesis of the Tianbaoshan carbonate-hosted Pb-Zn deposit, Southwest China: Geologic and isotopic (C-H-O-S-Pb) evidence. Inter. Geol. Rev. 55, 1300–1310.
Zhou, J.X., Luo, K., Wang, X.C., Wilde, S.A., Wu, T., Huang, Z.L., Cui, Y.L., Zhao, J.X., 2018c. Ore genesis of the Fule Pb-Zn deposit and its relationship with the Emeishan Large Igneous Province: Evidence from mineralogy, bulk C-O-S and in situ S-Pb isotopes. Gondwana Res. 54, 161–179.
Zhou, M.F., Malpas, J., Song, X.Y., Robinson, P.T., Sun, M., Kennedy, A.K., Lesher, C.M., Keays, R.R., 2002. A temporal link between the Emeishan large igneous province (SW China) and the end-Guadalupian mass extinction. Earth Planet. Sci. Lett. 196 (3–4), 113–122.
Zhou, J.X., Wang, X.C., Wilde, S.A., Luo, K., Huang, Z.L., Wu, T., Jin, Z.G., 2018a. New insights into the metallogeny of MVT Zn-Pb deposits: A case study from the Nayongzhi in South China, using field data, fluid compositions, and in situ S-Pb isotopes. Amer. Miner. 103, 91–108.
Zhou, J.X., Xiang, Z.Z., Zhou, M.F., Feng, Y.X., Luo, K., Huang, Z.L., Wu, T., 2018b. The giant Upper Yangtze Pb-Zn province in SW China: Reviews, new advances and a new genetic model. J. Asian Earth Sci. 154, 280–315.
Zhou, J.X., Huang, Z.L., Zhou, M.F., Zhu, X.K., Muchez, P., 2014a. Zinc, sulfur and lead isotopic variations in carbonate-hosted Pb-Zn sulfide deposits, southwest China. Ore Geol. Rev. 58, 41–54.
Zhou, J.X., Huang, Z.L., Lv, Z.C., Zhu, X.K., Gao, J.G., Mirnejad, H., 2014b. Geology, isotope geochemistry and ore genesis of the Shanshulin carbonate-hosted Pb–Zn deposit, southwest China. Ore Geol. Rev. 63, 209–225.
Zhou, J.X., Bai, J.H., Huang, Z.L., Zhu, D., Yan, Z.F., Lv, Z.C., 2015. Geology, isotope geochemistry and geochronology of the Jinshachang carbonate-hosted Pb-Zn deposit, South China. J. Asian Earth Sci. 98, 272–284.
Zhu, C., Wen, H., Zhang, Y., Fan, H., 2016. Cadmium and sulfur isotopic compositions of the Tianbaoshan Zn-Pb-Cd deposit, Sichuan Province, China. Ore Geol. Rev. 76, 152–162.
Zhu, C., Liao, S., Wang, W., Zhang, Y., Yang, T., Fan, H., Wen, H., 2018. Variations in Zn and S isotope chemistry of sedimentary sphalerite, Wusihe Zn-Pb deposit, Sichuan Province, China. Ore Geol. Rev. 95, 639–648.